First-principles predictions of temperature-dependent infrared dielectric function of polar materials by including four-phonon scattering and phonon frequency shift

Zhen Tong,[1,2] Xiaolong Yang,[3] Tianli Feng,[4] Hua Bao,[2,*] and Xiulin Ruan[1,†]

[1]*School of Mechanical Engineering and the Birck Nanotechnology Center, Purdue University, West Lafayette, Indiana 47907-2088, USA*

[2]*University of Michigan-Shanghai Jiao Tong University Joint Institute, Shanghai Jiao Tong University, Shanghai 200240, China*

[3]*Institute for Advanced Study, Shenzhen University, Nanhai Avenue 3688, Shenzhen 518060, China*

[4]*Materials Science and Technology Division, Oak Ridge National Laboratory, Oak Ridge, Tennessee 37831, USA*

(Received 13 September 2019; revised manuscript received 20 January 2020; accepted 30 January 2020; published 16 March 2020)

Recently, first-principles calculations based on density functional theory have been widely used to predict the temperature-dependent infrared spectrum of polar materials, but the calculations are usually limited to the harmonic frequency (0 K) and three-phonon scattering damping for the zone-center infrared-active optical phonon modes, and fail to predict the high-temperature infrared optical properties of materials such as sapphire (α-Al_2O_3), GaAs, TiO_2, etc., due to the neglect of high-order phonon scattering damping and phonon frequency shift. In this work, we implemented first-principles calculations to predict the temperature-dependent infrared dielectric function of polar materials by including four-phonon scattering and phonon frequency shift. The temperature-dependent phonon damping by including three- and four-phonon scattering as well as the phonon frequency shift by including cubic and quartic anharmonicity and the thermal expansion effect are calculated based on anharmonic lattice dynamics method. The infrared dielectric function of α-Al_2O_3 is parameterized, and then the temperature-dependent infrared optical reflectance is determined. We find that our predictions agree better with the experimental data than the previous density functional theory-based methods. This work will help to effectively predict the thermal radiative properties of polar materials at elevated temperature, which is generally difficult to measure, and will enable predictive design of new materials for radiative applications.

DOI: 10.1103/PhysRevB.101.125416

I. INTRODUCTION

Infrared (IR) optical properties have many important applications such as infrared detectors, radiative cooling, radiative heat transfer, and thermal light-emitting sources, and has attracted much research interest [1–10]; particularly, many works [11–14] have concerned the temperature-dependent optical property due to high-temperature applications. Recently, the density functional theory (DFT) based first-principles method has been extensively used to predict the temperature-dependent infrared dielectric spectrum of polar materials. However, only the harmonic frequency (0 K) and three-phonon scattering damping were considered for the zone-center IR-active optical phonon modes among these predictions, which results in underestimated damping [15,16] and unshifted frequency [7,9,14] compared to experimental data at finite temperature. To overcome these limitations, extensive theoretical works [17–20] calculating the temperature-dependent frequency shift and linewidth were conducted, and the formulas were given; however, their applications are limited to the experimental fitting formulas [17,18] or simple models [19,20]. On the other hand, the *ab initio* molecular dynamics (AIMD) approach [5] has been used to predict the IR optical properties of polar materials, which has the ability to include higher-order anharmonic effects on the optical phonon damping and frequency. However, AIMD still did not improve the results, probably due to the simulation domain size effect in MD, which is limited by computational cost. Furthermore, Yang *et al.* [10] improved the DFT-based first-principles methods to investigate the infrared optical properties of polar materials, in which the four-phonon scattering based on the Feng-Ruan four-phonon scattering formalism [21] was included in the phonon damping. Their predictions agree well with experimental values after including the four-phonon scattering damping at high temperature for quite harmonic materials (BAs, cubic SiC, α-SiO_2). However, for materials such as α-Al_2O_3, GaAs, TiO_2, etc., the neglect of the phonon frequency shift may still lead to significant inaccuracy. Recently, Fugallo *et al.* [22] predicted the temperature-dependent optical properties of MgO by considering the frequency shift and four-phonon damping of the zone-center optical phonon mode based on the density functional perturbation theory (DFPT) "$2n + 1$" approach, in which the frequency-dependent phonon damping was predicted. On the other hand, some recent works considered both four-phonon scattering and the phonon frequency shift in the thermal conductivity prediction [23,24] with the quartic anharmonic force constants for arbitrary $\mathbf{q}$ points in the Brillouin zone, but the phonon frequency shift has not been employed for zone-center IR modes and thermal radiative properties yet. Therefore, fully first principles

*hua.bao@sjtu.edu.cn
†ruan@purdue.edu

calculations are necessary to obtain the four-phonon linewidth and quartic anharmonic frequency shift of arbitrary **q** points in the Brillouin zone, and then capture the temperature-dependent features of the optical phonon frequency and damping for predicting the IR spectrum of polar materials.

In addition to numerical simulations, extensive experimental measurements have been widely carried out to obtain the finite temperature optical properties of polar materials using different techniques such as a double-pass Perkin Elmer spectrometer [1], a Fourier transform infrared (FTIR) spectrometer [25], ellipsometry [26], etc. However, these measurements are hard to perform at high temperature (over 1000 K) due to the limitation of self-radiation and thermal oxidation [26]. Also, it is difficult to separate the temperature-dependent factor including three- and four-phonon or even higher-order scattering as well as a phonon frequency shift based on these directly experimental measurements.

In this work, we will investigate comprehensive DFT-based first-principles calculations to predict the temperature-dependent IR optical properties of polar materials by including the four-phonon scattering and phonon frequency shift. The second-, third-, and fourth-order interatomic force constants (second, third, and fourth IFCs) are computed by using finite-difference methods based on first-principles calculations for the determination of the three- and four-phonon scattering damping. The third and fourth IFCs and thermal expansion coefficient are calculated to capture the frequency shift stemming from cubic (three-phonon scattering) and quartic (four-phonon scattering) anharmonicity and thermal expansion. Finally, the calculated temperature-dependent IR optical phonon frequency and damping are used to parametrize the dielectric function and then predict the IR optical properties. α-Al_2O_3 is used as an example material in the present work.

II. METHODOLOGY AND SIMULATION DETAILS

The dielectric function model used for describing the dielectric properties of α-Al_2O_3 can be written in the form [27–29]

$$\epsilon(\omega) = \epsilon_\infty \prod_j \frac{\omega_{j,\mathrm{LO}}^2 - \omega^2 + i\gamma_{j,\mathrm{LO}}\omega}{\omega_{j,\mathrm{TO}}^2 - \omega^2 + i\gamma_{j,\mathrm{TO}}\omega}, \tag{1}$$

where ϵ_∞ is the high-frequency dielectric constant, ω_j is the resonance frequency, and LO and TO denote the longitudinal and transverse IR phonon modes, respectively. j goes over all the IR-active modes, and γ_j is the damping factor of the jth resonance phonon mode.

From Eq. (1), the dielectric spectrum can be determined if the parameters (such as ω_j and γ_j) are known. Actually, the phonon frequency ω_j at finite temperature shifts away from the harmonic values due to anharmonicity and thermal expansion, which is not easy to determine directly from theoretical methods. Also, the phonon damping factor γ, the reciprocal of phonon lifetime (scattering rate) τ^{-1}, is hard to obtain from theoretical calculations, and is usually fitted from the experimentally measured reflectance [28] or extracted from measured Raman linewidths [30].

A. Phonon frequency shift

In general, at finite temperature, the frequency shift originating from anharmonicity (phonon scattering) is given by the real part of the self-energy [18]. In the phonon frequency shift, the three-phonon scattering contributes to the second-order bubble diagram, while the four-phonon scattering contributes to the first-order loop diagram [17,18,31,32]. The three- and four-phonon terms in the frequency shift can be calculated by [18,33]

$$\Delta\omega_\lambda^{3\mathrm{ph}} = \frac{\hbar}{16N_{\mathbf{q}}\omega_\lambda}\sum_{\lambda_1\lambda_2}\left[\left|V^{3\mathrm{ph}}_{\lambda-\lambda_1-\lambda_2}\right|^2\delta_{\mathbf{q}-\mathbf{q}_1-\mathbf{q}_2}\frac{n_1+n_2+1}{\omega_1\omega_2(\omega_\lambda-\omega_1-\omega_2)_P} + 2\left|V^{3\mathrm{ph}}_{\lambda-\lambda_1-\lambda_2}\right|^2\delta_{\mathbf{q}+\mathbf{q}_1-\mathbf{q}_2}\frac{n_1-n_2}{\omega_1\omega_2(\omega_\lambda+\omega_1-\omega_2)_P}\right], \tag{2}$$

$$\Delta\omega_\lambda^{4\mathrm{ph}} = \frac{\hbar}{8N_{\mathbf{q}}\omega_\lambda}\sum_{\lambda_1}V^{4\mathrm{ph}}_{-\lambda\lambda\lambda_1-\lambda_1}\frac{2n_1+1}{\omega_1}, \tag{3}$$

where $\hbar$ is the reduced Planck constant, $N_{\mathbf{q}}$ is the number of **q** points in the Brillouin zone, ω is the frequency, and $n = (e^{\hbar\omega/k_BT}-1)^{-1}$ is the phonon occupation number. $V_{\pm}^{3\mathrm{ph}}$ and $V_{\pm\pm}^{4\mathrm{ph}}$ are the three- and four-phonon scattering matrices given by [21]

$$V^{3\mathrm{ph}}_{\lambda\lambda_1\lambda_2} = \sum_{b,l_1b_1,l_2b_2}\sum_{\alpha\alpha_1\alpha_2}\Psi^{\alpha\alpha_1\alpha_2}_{0b,l_1b_1,l_2b_2}\frac{e^{\lambda}_{\alpha b}e^{\lambda_1}_{\alpha_1 b_1}e^{\lambda_2}_{\alpha_2 b_2}}{\sqrt{\bar{m}_b\bar{m}_{b_1}\bar{m}_{b_2}}}e^{i(\mathbf{k}_1\cdot\mathbf{r}_{l_1}+\mathbf{k}_2\cdot\mathbf{r}_{l_2})}, \tag{4}$$

$$V^{4\mathrm{ph}}_{\lambda\lambda_1\lambda_2\lambda_3} = \sum_{b,l_1b_1,l_2b_2,l_3b_3}\sum_{\alpha\alpha_1\alpha_2\alpha_3}\Phi^{\alpha\alpha_1\alpha_2\alpha_3}_{0b,l_1b_1,l_2b_2,l_3b_3}\frac{e^{\lambda}_{\alpha b}e^{\lambda_1}_{\alpha_1 b_1}e^{\lambda_2}_{\alpha_2 b_2}e^{\lambda_3}_{\alpha_3 b_3}}{\sqrt{\bar{m}_b\bar{m}_{b_1}\bar{m}_{b_2}\bar{m}_{b_3}}} \times e^{i(\mathbf{k}_1\cdot\mathbf{r}_{l_1}+\mathbf{k}_2\cdot\mathbf{r}_{l_2}+\mathbf{k}_3\cdot\mathbf{r}_{l_3})}, \tag{5}$$

where l, b, and α denote the indexes of unit cells, basis atoms, and the (x, y, z) directions, respectively. $\mathbf{r}_l$ is the position of the primitive cell l, m is the mass of an atom, e is the phonon eigenvector, and Ψ and Φ are the third and fourth IFCs.

On the other hand, the effect of thermal expansion may be taken into account by considering ω_λ^0 as the quasiharmonic frequency $\omega_\lambda^{\mathrm{quasi}}$, in which the temperature-dependent lattice constant or thermal expansion is included. Thus, the temperature-dependent frequency shift due to thermal expansion is given by [33,34]

$$\begin{aligned}\Delta\omega_\lambda^{\mathrm{quasi}} &= \omega_\lambda^{\mathrm{quasi}} - \omega_\lambda^0 \\ &= \omega_\lambda^0\left\{\exp\left[\int_0^T \alpha_V(T)dT\right]^{-g_\lambda} - 1\right\}.\end{aligned} \tag{6}$$

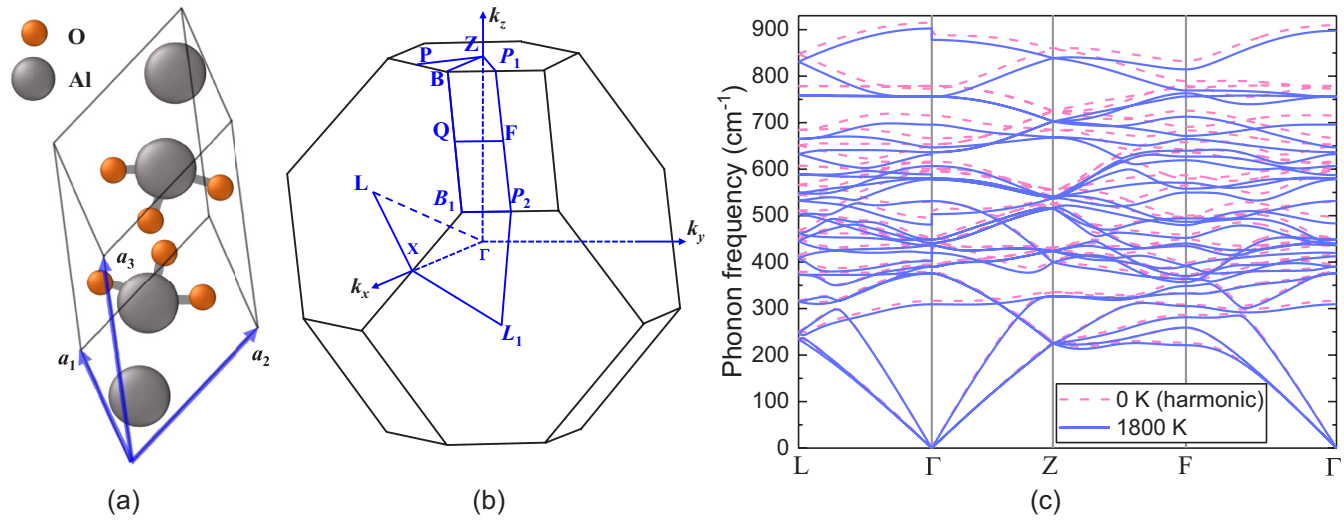

FIG. 1. (a) Crystal structure of the primitive unit cell of α-Al_2O_3, which contains four aluminum atoms (gray) and six oxygen atoms (orange). The $\boldsymbol{a}_1$, $\boldsymbol{a}_2$, and $\boldsymbol{a}_3$ are the primitive lattice vectors. (b) First Brillouin zone of α-Al_2O_3. The high-symmetry notations are referred to Ref. [41]. (c) Temperature-dependent phonon dispersion curve of α-Al_2O_3 calculated from first principles. The harmonic frequency (dashed pink line, at 0 K) corresponding to ω_λ^0 and the anharmonic frequency (solid blue line, at 1800 K) corresponding to $\omega_\lambda^0 + \Delta\omega_\lambda^{3\text{ph}} + \Delta\omega_\lambda^{4\text{ph}} + \Delta\omega_\lambda^{\text{quasi}}$ are shown to compare the temperature effect.

α_V is the temperature-dependent thermal expansion coefficient given by

$$\alpha_V(T) = -\frac{k_B}{N_{\mathbf{q}} V B} \sum_\lambda g_\lambda \left(\frac{x}{2}\right)\left[1 - \coth^2\left(\frac{x}{2}\right)\right], \quad (7)$$

where V is the volume of the primitive, k_B is the Boltzmann constant, and $x = \hbar\omega/k_B T$. $g_\lambda = -\frac{V}{\omega_\lambda^0}\frac{\partial \omega_\lambda^0}{\partial V}$ is the Grüneisen parameter, and $B = -V\frac{dP}{dV}$ is the bulk modulus.

Finally, the temperature-dependent phonon frequency of a certain phonon mode λ can be obtained as

$$\omega_\lambda(T) = \omega_\lambda^0 + \Delta\omega_\lambda^{3\text{ph}} + \Delta\omega_\lambda^{4\text{ph}} + \Delta\omega_\lambda^{\text{quasi}}. \quad (8)$$

B. Phonon damping with three- and four-phonon scattering

In general, the phonon damping γ (or scattering rate τ^{-1}) can be calculated through the anharmonic lattice method, in which the harmonic and anharmonic interatomic force constants are determined from first-principles calculations [9]. Here, both three- and four-phonon scattering are included in the phonon damping calculations. Based on Fermi's golden rule [35], $\gamma_\lambda^{3\text{ph}}$ due to the three-phonon scattering rate $\tau_{3\text{ph},\lambda}^{-1}$ can be calculated by the summations of the probabilities of all possible three-phonon scattering events with the single-mode relaxation time approximation (SMRTA) [18,35],

$$\gamma_\lambda^{3\text{ph}} = \tau_{3\text{ph},\lambda}^{-1} = \left(\sum_{\lambda_1\lambda_2} \Gamma_{\lambda\lambda_1}^{\lambda_2} + \frac{1}{2}\sum_{\lambda_1\lambda_2} \Gamma_\lambda^{\lambda_1\lambda_2}\right), \quad (9)$$

where λ_1 and λ_2 denote the second and third phonon modes that scatter with phonon mode λ. $\Gamma_{\lambda\lambda_1}^{\lambda_2}$ and $\Gamma_\lambda^{\lambda_1\lambda_2}$ represent the intrinsic three-phonon scattering rates for absorption processes $\lambda + \lambda_1 \to \lambda_2$ and emission processes $\lambda \to \lambda_1 + \lambda_2$, respectively.

Similarly, $\gamma_\lambda^{4\text{ph}}$ due to the four-phonon scattering rate $\tau_{4\text{ph},\lambda}^{-1}$ including all possible four-phonon interaction events can be obtained based on SMRTA [10,21],

$$\gamma_\lambda^{4\text{ph}} = \tau_{4\text{ph},\lambda}^{-1} = \left(\frac{1}{6}\sum_{\lambda_1\lambda_2\lambda_3} \Gamma_\lambda^{\lambda_1\lambda_2\lambda_3} + \frac{1}{2}\sum_{\lambda_1\lambda_2\lambda_3} \Gamma_{\lambda\lambda_1}^{\lambda_2\lambda_3} + \frac{1}{2}\sum_{\lambda_1\lambda_2\lambda_3} \Gamma_{\lambda\lambda_1\lambda_2}^{\lambda_3}\right). \quad (10)$$

Finally, the phonon damping γ_λ of the phonon mode λ can be obtained by including both three- and four-phonon scattering rates based on SMRTA,

$$\gamma_\lambda^{3+4\text{ph}} = \frac{1}{\tau_\lambda^{3+4\text{ph}}} = \tau_{3\text{ph},\lambda}^{-1} + \tau_{4\text{ph},\lambda}^{-1}. \quad (11)$$

From the above derivations, all the parameters in Eq. (1) will be determined if the second, third, and fourth IFCs are provided. Here, the IFCs of α-Al_2O_3 were predicted from first-principles calculations, which were carried out in VASP [36]. The local-density approximation [37] with the projector augmented-wave method [38] was used for exchange and correlation functionals. The plane-wave energy cutoff is 520 eV, the energy convergence threshold is set at 10^{-8} eV, and the electron **k** mesh is set as $3 \times 3 \times 3$. The lattice structure of α-Al_2O_3 belongs to the trigonal system (space group $R\bar{3}c$), which has a rhombohedral primitive unit cell containing 2 f.u. (10 atoms), as shown in Fig. 1(a). The optimized lattice parameters are $a = 5.140$ Å and $\alpha = 55.35°$ (experimental values [14] are $a = 5.128$ Å and $\alpha = 55.28°$). The second IFCs and harmonic phonon frequencies were extracted by using PHONOPY [39], which was interfaced with VASP [36], in which the $3 \times 3 \times 3$ primitive cell was used to perform the DFPT calculations. The third IFCs were calculated by using the code THIRDORDER.PY from the package ShengBTE [40] based on VASP, in which the supercell was taken to be a $3 \times 3 \times 3$ primitive cell and the cutoff radius was considered up to fourth-nearest-neighbor atoms. The fourth IFCs

were calculated by using the in-house code developed based on THIRDORDER.PY [40], in which the third-nearest-neighbor cutoff was considered using a $3 \times 3 \times 3$ primitive cell. The $18 \times 18 \times 18$ **q** points were used for the integration of the Brillouin zone based on careful convergence calculations. The three-phonon scattering rate was calculated by using ShengBTE [40], while the four-phonon scattering rate was computed using the in-house code [21]. Also, the frequency shift due to four-phonon scattering and thermal expansion was calculated by using our in-house code [33].

III. RESULTS AND DISCUSSION

A. Temperature-dependent phonon frequency

α-Al_2O_3 has a hexagonal conventional unit cell crystal structure with a rhombohedral primitive unit cell, as shown in Fig. 1(a), which results in an anisotropic feature itself. In general, the anisotropic dielectric of α-Al_2O_3 can be distinguished with an ordinary ray spectrum (incident light with the electric vector perpendicular to the z axis) and an extraordinary ray spectrum (incident light with the electric vector parallel to the z axis). It should be noted that there are multiple optical phonon modes in α-Al_2O_3, which are denoted as $2A_{1g} + 2A_{1u} + 3A_{2g} + 2A_{2u} + 4E_u + 5E_g$ based on symmetry analysis [42,43]. Among these modes, the A_{2u} (extraordinary ray) and E_u (ordinary ray) species are IR-active modes, A_{1g} and E_g are Raman-active modes, and A_{2g} and A_{1u} are spectroscopically inactive [43]. In addition, the frequency of TO and LO branches at the zone center ($\mathbf{k} = 0$) of these IR-active modes depends on the direction in reciprocal space. For example, along the direction of $\Gamma \rightarrow \mathbf{X}$ (in the xy plane), as shown in Fig. 1(b), the frequency is that of a LO component of E_u or a TO component of A_{2u}; along the direction of $\Gamma \rightarrow \mathbf{Z}$ (z axis), the frequency is that of a TO component of E_u or a LO component of A_{2u}. Based on these theories, the TO and LO branch indexes of the A_{2u} and E_u modes are determined using PHONOPY [39].

Figure 1(c) shows the phonon dispersion spectrum along the high-symmetry points in the first Brillouin zone, as denoted in Fig. 1(b) at 0 and 1800 K. From Fig. 1(c), we can see that the phonon frequency decreases as temperature increases, which is mainly due to the positive Grüneisen parameters and thermal expansion coefficients in α-Al_2O_3. We can also see that the frequency shift in optical modes is significant, which is particularly important in determining the dielectric spectrum, especially at elevated temperature. Moreover, this result indicates that the overall temperature effect on the vibrational frequencies can be successfully captured for the whole Brillouin zone based on our method.

On the other hand, the temperature-dependent reflectance spectrum for an ordinary ray of α-Al_2O_3 was experimentally determined in Piriou's work [28]. Based on this reflectance spectrum, the temperature-dependent phonon frequencies of the IR phonon modes were further fitted by using the dielectric model of Eq. (1) in Gervais and Piriou's work [28]. Although they obtained the finite-temperature IR phonon modes' frequencies, the thermal expansion and purely anharmonic effects in the observed frequency shifts were not possible to separate, as claimed in their work [28]. However, in our work, the frequency shifts due to thermal expansion and quartic anharmonicity effects are separately calculated from first-principles calculations.

Finally, the temperature-dependent phonon frequencies of E_u species IR-active modes calculated using our method based on first-principles calculations are compared with the experimental fitting data in Ref. [28], which are shown in Fig. 2. We can see that our calculated temperature-dependent phonon frequencies ($\omega_\lambda^0 + \Delta\omega_\lambda^{3\text{ph}} + \Delta\omega_\lambda^{4\text{ph}} + \Delta\omega_\lambda^{\text{quasi}}$) agree well with the experimental data in general. Actually, it can be found that our predictions are underestimated compared to experimental values, which might be improved if the higher than fourth order anharmonic frequency shift is included. It can also be seen that the frequency shifts are negative due to thermal expansion ($\Delta\omega_\lambda^{\text{quasi}}$) but are positive due to four-phonon anharmonicity ($\Delta\omega_\lambda^{4\text{ph}}$). Also, it should be noted that the four-phonon anharmonicity makes the major contribution to the frequency shift, and it is generally much larger than that of three-phonon anharmonicity, which is similar to the conclusion in Refs. [32,33]. Moreover, the magnitude of $\Delta\omega_\lambda^{\text{quasi}}$ is larger than that of $\Delta\omega_\lambda^{4\text{ph}}$, which indicates that the thermal expansion is the predominant effect on the frequency shift, and this predominance finally results in the negative total frequency shift. The softening of these phonon modes are mainly due to the positive Grüneisen parameters and thermal expansion coefficients in α-Al_2O_3. In addition, the magnitude of the frequency shift increases with increasing temperature, which indicates the temperature effect on vibrational frequencies is significant, especially at elevated temperature.

B. Temperature-dependent phonon damping

The temperature-dependent three-phonon ($\gamma_\lambda^{3\text{ph}}$) and four-phonon ($\gamma_\lambda^{4\text{ph}}$) scattering dampings of the IR-active phonon modes in α-Al_2O_3 are shown in Fig. 3. We can see that $\gamma_\lambda^{3\text{ph}}$ dominates at low to intermediate temperatures, but $\gamma_\lambda^{4\text{ph}}$ can become non-negligible or even comparable to $\gamma_\lambda^{3\text{ph}}$ for some modes at high temperature (~1800 K), which indicates that the four-phonon scattering contribution to the phonon damping is significant due to the strong anharmonic phonon-phonon scattering at elevated temperature. On the other hand, we can see that the phonon damping scales with temperature as $\gamma_\lambda^{3\text{ph}} \sim T$ and $\gamma_\lambda^{4\text{ph}} \sim T^2$. Hence, we can write the total phonon damping $\gamma = A + BT + CT^2 + \ldots$, in which the coefficients A, B, and C are related to isotope, three- and four-phonon scattering, respectively. This formula is useful to understand different damping mechanisms in the total damping factor obtained through experiments or modeling (such as molecular dynamics).

C. Temperature-dependent reflectance spectrum

The high-frequency dielectric constant ϵ_∞ is calculated from first-principles with values of $\epsilon_\infty^{\parallel} = 3.21$ (ordinary ray) and $\epsilon_\infty^{\perp} = 3.20$ (extraordinary ray), which agree well with the experimental values of $\epsilon_\infty^{\parallel} = 3.2$ and $\epsilon_\infty^{\perp} = 3.1$ [2]. Finally, by inserting the obtained high-frequency dielectric constant ϵ_∞, temperature-dependent phonon frequency ω_λ, and damping γ_λ

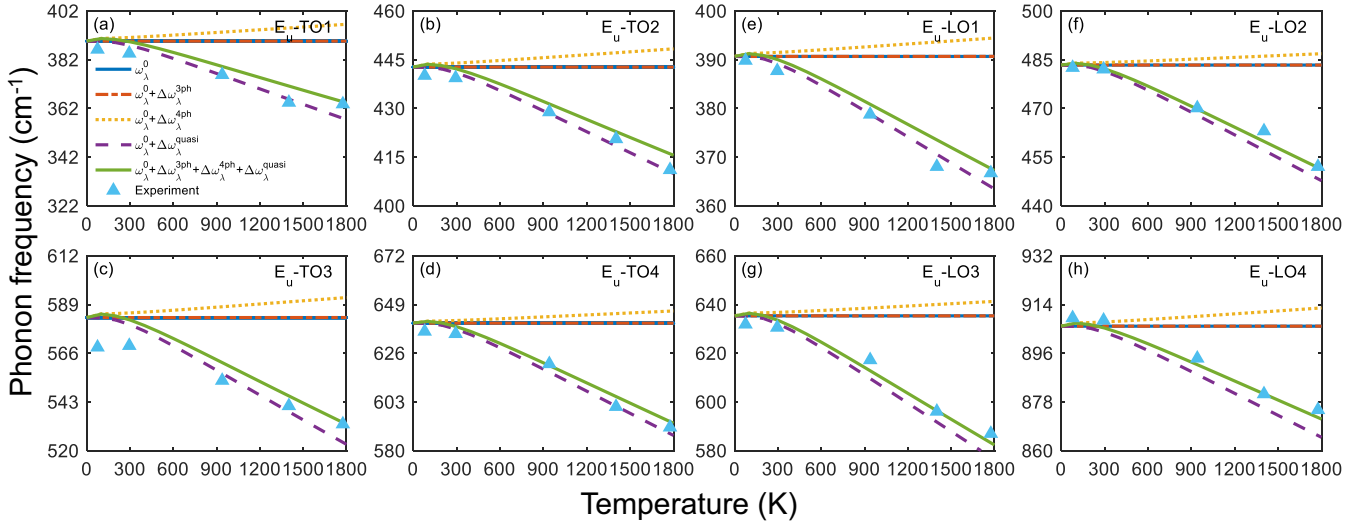

FIG. 2. The temperature-dependent phonon frequency calculated from first principles as compared with experimental data. The IR-active optical mode with a symmetry of E_u, which includes four species in α-Al_2O_3 at the Γ point, is calculated in this work. The frequency shift effect on harmonic frequency (solid blue line labeled ω_λ^0) due to three-phonon scattering (dot-dashed brown line labeled $\omega_\lambda^0 + \Delta\omega_\lambda^{3ph}$), four-phonon scattering (dotted yellow line labeled $\omega_\lambda^0 + \Delta\omega_\lambda^{4ph}$), thermal expansion (dashed purple line labeled $\omega_\lambda^0 + \Delta\omega_\lambda^{quasi}$), and total effects (solid green line labeled $\omega_\lambda^0 + \Delta\omega_\lambda^{3ph} + \Delta\omega_\lambda^{4ph} + \Delta\omega_\lambda^{quasi}$) is calculated for (a)–(d) TO and (e)–(h) LO modes. The experimental data [28] (triangles) fitted from the experimental measurements of reflectance of α-Al_2O_3 are shown for comparison.

of the IR-active modes into the dielectric function in Eq. (1), the temperature-dependent dielectric function is determined. Furthermore, the temperature-dependent semi-infinite normal reflectance R can be determined with the relation

$$R = \left\{\sqrt{\epsilon_1^2+\epsilon_2^2}+1-\sqrt{2\left(\sqrt{\epsilon_1^2+\epsilon_2^2}+\epsilon_1\right)}\right\}/ \times \left\{\sqrt{\epsilon_1^2+\epsilon_2^2}+1+\sqrt{2\left(\sqrt{\epsilon_1^2+\epsilon_2^2}+\epsilon_1\right)}\right\},$$

in which ϵ_1 and ϵ_2 are the real and imaginary parts of ϵ, respectively.

The temperature-dependent reflectance spectrum (ordinary ray) of α-Al_2O_3 is shown in Fig. 4 at 77 and 1775 K. At low temperature (77 K) in Fig. 4(a), it can be seen that the effect of the frequency shift and four-phonon scattering damping on the reflectance is not significant. However, at high temperature (1775 K) in Fig. 4(b), the reflectance calculated using γ_λ^{3+4ph} with ω_λ^0 (dashed yellow line) reduces the reflectance peak compared to the curve using γ_λ^{3ph} with ω_λ^0 (dotted red line), but

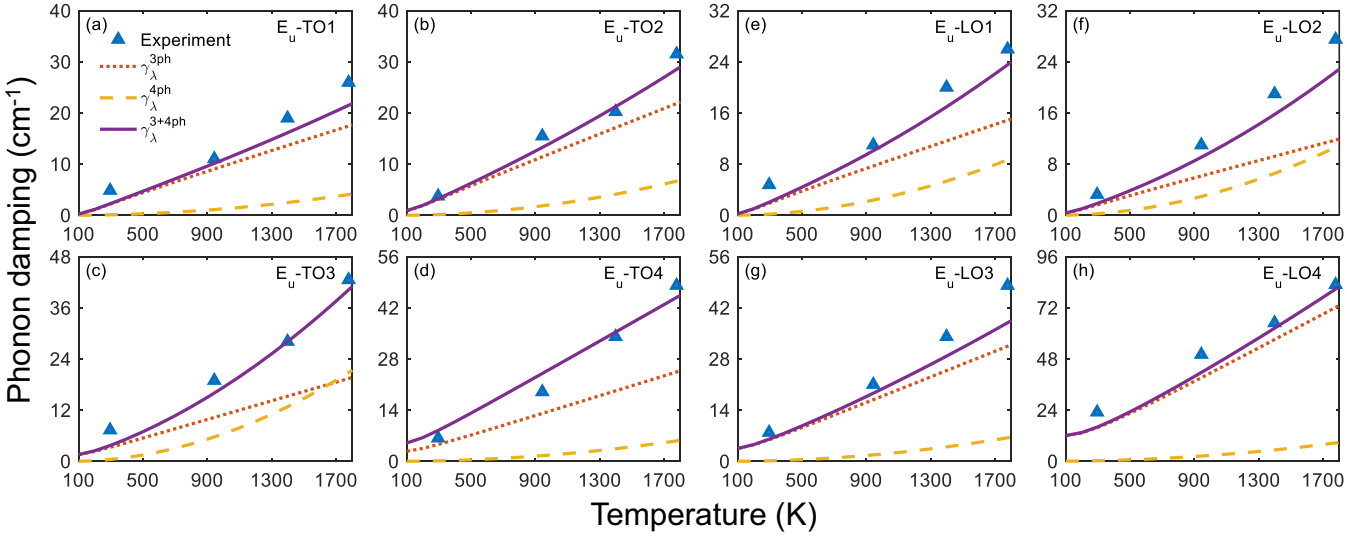

FIG. 3. The temperature-dependent phonon damping γ calculated from first-principles as compared with experimental data. The γ of the IR-active optical mode with a symmetry of E_u, which includes four species in α-Al_2O_3 at the Γ point, is calculated in this work. The γ_λ^{3ph} (dotted red line) and γ_λ^{4ph} (dashed yellow line) due to three- and four-phonon scattering are shown as a function of temperature for (a)–(d) TO and (e)–(h) LO modes. The experimental data [28] (triangles) fitted from the experimental measurements of reflectance of α-Al_2O_3 are shown for comparison with the calculated total phonon damping γ_λ^{3+4ph} (solid purple line).

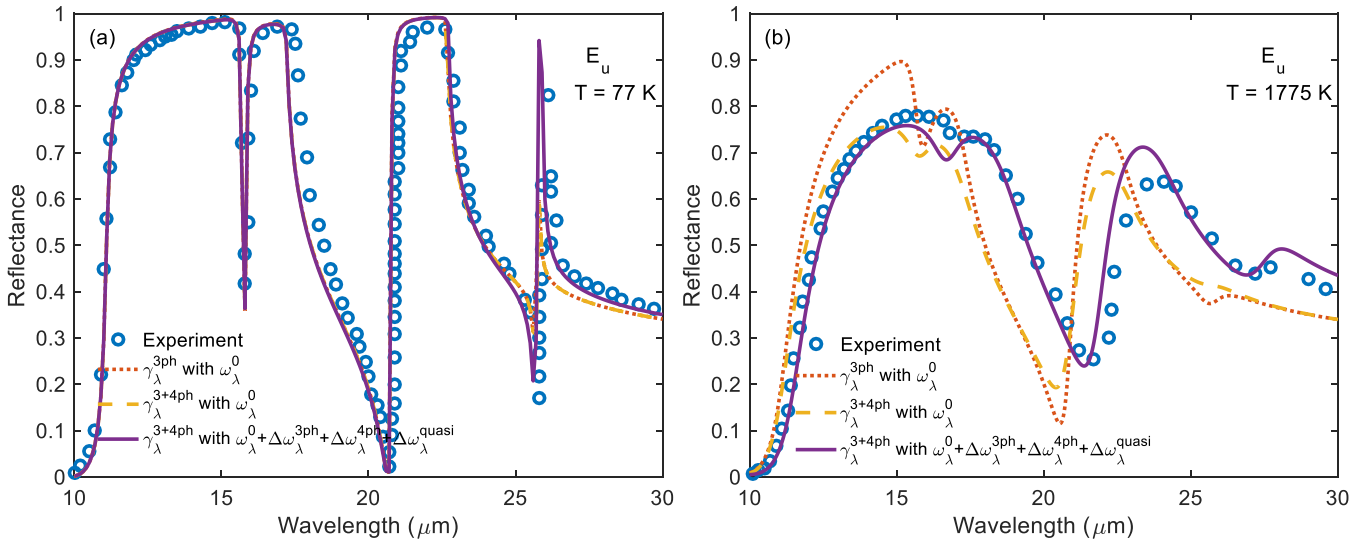

FIG. 4. The semi-infinite normal reflectance calculated from first principles as compared with experimental data. The temperature-dependent reflectance spectrum (ordinary ray) of α-Al_2O_3 is shown (a) at 77 K and (b) at 1775 K. The reflectances calculated using γ_λ^{3ph} with ω_λ^0 (dotted red line), γ_λ^{3+4ph} with ω_λ^0 (dashed yellow line), and γ_λ^{3+4ph} with $\omega_\lambda^0 + \Delta\omega_\lambda^{3ph} + \Delta\omega_\lambda^{4ph} + \Delta\omega_\lambda^{quasi}$ (solid purple line) are plotted for comparison with experimental data [28] (blue circles).

there still exists a peak shift deviating from the experimental data. Meanwhile, after including the frequency shift and plotting the reflectance using γ_λ^{3+4ph} with $\omega_\lambda^0 + \Delta\omega_\lambda^{3ph} + \Delta\omega_\lambda^{4ph} + \Delta\omega_\lambda^{quasi}$, the reflectance spectrum denoted by the dashed yellow line becomes the solid purple line, as shown in Fig. 4(b), which results in excellent agreement with experimental data. This result indicates that the frequency shift is necessary in the dielectric function prediction at high temperature. Our method improved the previous methods which did not consider the phonon frequency shift [10], thus resulting in the prediction inaccuracy of the optical properties for strongly anharmonic materials at high temperature.

On the other hand, the extraordinary reflectance spectrum at room temperature is also calculated, and it is compared with the experimental measurements [2], which is shown in Fig. 5. We can see that the calculated reflectance including the frequency shift and four-phonon scattering damping matches the experimental data well overall. All of these results give confidence to our method of predicting the temperature-dependent IR dielectric function of polar materials by including the four-phonon scattering and phonon frequency shift.

IV. CONCLUSIONS

In summary, by performing the DFT-based first-principles calculations, we predicted the temperature-dependent IR dielectric function of polar materials by including the four-phonon scattering and phonon frequency shift. α-Al_2O_3 was used as an example material in this work. The three- and four-phonon scattering effect on phonon damping and the cubic and quartic anharmonicity and thermal expansion effect on frequency shift were calculated based on the anharmonic lattice method with perturbation theory to predict the temperature-dependent IR optical properties. Our predictions are in excellent agreement with the reported experimental data. Based on the analysis of the effects of three- and four-phonon scattering on the phonon damping separately, we found that the four-phonon scattering damping is comparable to three-phonon scattering damping at high temperature for some infrared phonon modes in α-Al_2O_3. We also found that the phonon frequency is softened due to thermal expansion and is hardened due to quartic anharmonicity, but the former dominates and finally results in a total negative frequency shift in α-Al_2O_3. Using these obtained temperature-dependent

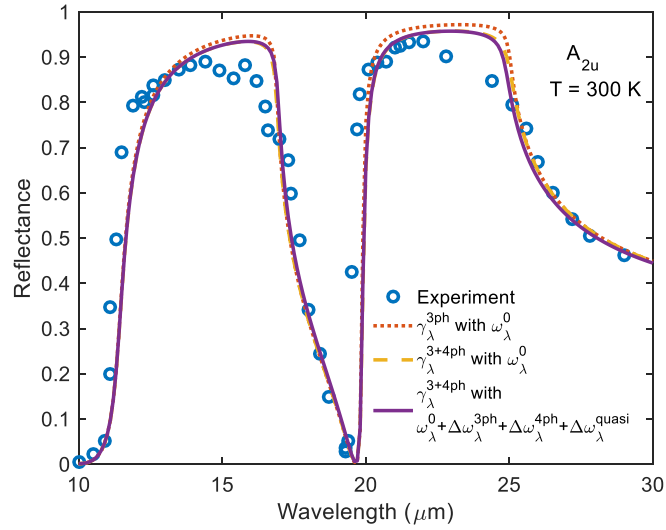

FIG. 5. The semi-infinite normal reflectance calculated from first principles as compared with experimental data. The temperature-dependent reflectance spectrum (extraordinary ray) of α-Al_2O_3 is shown at 300 K. The reflectances calculated using γ_λ^{3ph} with ω_λ^0 (dotted red line), γ_λ^{3+4ph} with ω_λ^0 (dashed yellow line), and γ_λ^{3+4ph} with $\omega_\lambda^0 + \Delta\omega_\lambda^{3ph} + \Delta\omega_\lambda^{4ph} + \Delta\omega_\lambda^{quasi}$ (solid purple line) are plotted for comparison with experimental data [2] (blue circles).

infrared optical phonon properties to parametrize the infrared dielectric function, the predicted semi-infinite reflectance agrees better with the experimental values than previous DFT-based methods. This method paves the way for effectively modeling the temperature-dependent optical properties of polar materials, which are generally not easy to obtain through experimental measurements, especially at high temperatures. Therefore, it enables predictive design of new materials for radiative applications.

ACKNOWLEDGMENTS

Simulations were performed at the Rosen Center for Advanced Computing (RCAC) of Purdue University. X.R. acknowledges the partial support from the National Science Foundation (Award No. 1150948). H.B. acknowledges the support from the National Natural Science Foundation of China (Grant No. 51676121). Z.T. is also thankful for the financial support of the Chinese Scholarship Council (CSC, Grant No. 201806230169).

[1] W. G. Spitzer, D. A. Kleinman, and C. J. Frosch, Phys. Rev. **113**, 133 (1959).
[2] A. S. Barker, Phys. Rev. **132**, 1474 (1963).
[3] F. Gervais and B. Piriou, Phys. Rev. B **11**, 3944 (1975).
[4] H. Bao and X. Ruan, Int. J. Heat Mass Transfer **53**, 1308 (2010).
[5] H. Bao, B. Qiu, Y. Zhang, and X. Ruan, J. Quant. Spectrosc. Radiat. Transfer **113**, 1683 (2012).
[6] J. Yang, M. Xu, and L. Liu, J. Quant. Spectrosc. Radiat. Transfer **184**, 111 (2016).
[7] A. Mock, R. Korlacki, S. Knight, and M. Schubert, Phys. Rev. B **95**, 165202 (2017).
[8] G. Domingues, A. M. Monthe, S. Guévelou, and B. Rousseau, J. Quant. Spectrosc. Radiat. Transfer **205**, 220 (2018).
[9] Z. Tong, L. Liu, L. Li, and H. Bao, Physica B (Amsterdam, Neth.) **537**, 194 (2018).
[10] X. Yang, T. Feng, J. S. Kang, Y. Hu, J. Li, and X. Ruan, arXiv:1908.05121.
[11] D. Olego and M. Cardona, Phys. Rev. B **25**, 3889 (1982).
[12] S. Dakshinamurthy, N. R. Quick, and A. Kar, J. Phys. D **40**, 353 (2007).
[13] K. M. Pitman, A. M. Hofmeister, A. B. Corman, and A. K. Speck, Astron. Astrophys. **483**, 661 (2008).
[14] J. Breeze, *Temperature and Frequency Dependence of Complex Permittivity in Metal Oxide Dielectrics: Theory, Modelling and Measurement*, Springer Theses (Springer, Cham, 2016).
[15] A. Debernardi, S. Baroni, and E. Molinari, Phys. Rev. Lett. **75**, 1819 (1995).
[16] A. Debernardi, Phys. Rev. B **57**, 12847 (1998).
[17] M. Balkanski, R. F. Wallis, and E. Haro, Phys. Rev. B **28**, 1928 (1983).
[18] A. A. Maradudin and A. E. Fein, Phys. Rev. **128**, 2589 (1962).
[19] M. R. Monga and K. N. Pathak, Phys. Rev. B **18**, 5859 (1978).
[20] P. Procacci, G. Cardini, R. Righini, and S. Califano, Phys. Rev. B **45**, 2113 (1992).
[21] T. Feng and X. Ruan, Phys. Rev. B **93**, 045202 (2016).
[22] G. Fugallo, B. Rousseau, and M. Lazzeri, Phys. Rev. B **98**, 184307 (2018).
[23] N. K. Ravichandran and D. Broido, Phys. Rev. B **98**, 085205 (2018).
[24] Y. Xia, Appl. Phys. Lett. **113**, 073901 (2018).
[25] P. R. Griffiths and J. A. D. Haseth, *Fourier Transform Infrared Spectrometry* (Wiley, Hoboken, NJ, 2007).
[26] H. Fujiwara, *Spectroscopic Ellipsometry* (Wiley, Chichester, 2007).
[27] A. S. Barker, Phys. Rev. **136**, A1290 (1964).
[28] F. Gervais and B. Piriou, J. Phys. C **7**, 2374 (1974).
[29] D. W. Berreman and F. C. Unterwald, Phys. Rev. **174**, 791 (1968).
[30] M. Ashkin, J. H. Parker, and D. W. Feldman, Solid State Commun. **6**, 343 (1968).
[31] M. Lazzeri, M. Calandra, and F. Mauri, Phys. Rev. B **68**, 220509(R) (2003).
[32] T. Tadano and S. Tsuneyuki, J. Phys. Soc. Jpn. **87**, 041015 (2018).
[33] T. Feng, X. Yang, and X. Ruan, J. Appl. Phys. **124**, 145101 (2018).
[34] U. Argaman, E. Eidelstein, O. Levy, and G. Makov, Phys. Rev. B **94**, 174305 (2016).
[35] G. D. Mahan, *Many-Particle Physics*, 3rd ed. (Kluwer Academic, New York, 2000).
[36] G. Kresse and J. Hafner, Phys. Rev. B **47**, 558 (1993).
[37] L. Hedin and B. I. Lundqvist, J. Phys. C **4**, 2064 (1971).
[38] G. Kresse and D. Joubert, Phys. Rev. B **59**, 1758 (1999).
[39] A. Togo and I. Tanaka, Scr. Mater. **108**, 1 (2015).
[40] W. Li, J. Carrete, N. A. Katcho, and N. Mingo, Comput. Phys. Commun. **185**, 1747 (2014).
[41] W. Setyawan and S. Curtarolo, Comput. Mater. Sci. **49**, 299 (2010).
[42] S. P. S. Porto and R. S. Krishnan, J. Chem. Phys. **47**, 1009 (1967).
[43] P. F. McMillan and N. L. Ross, Phys. Chem. Miner. **14**, 225 (1987).